

Effect of grain boundary on the crack-tip plasticity under hydrogen environment: an atomistic study

Kai Zhao^{1,2}, Jianying He¹, Zhiliang Zhang^{1*}

1 Department of Structural Engineering, Norwegian University of Science and Technology, 7491 Trondheim, Norway

2 Department of Engineering, Aarhus University, 8000 Aarhus C, Denmark

Abstract

It has been found that the plasticity is significantly affected by the hydrogen interstitials in metallic materials. However, the underlying physics responsible for the dislocation/hydrogen interactions is still poorly understood. Using molecular dynamics simulations, we study the emission of dislocations from a crack-tip in fcc Ni single crystal and bicrystal samples under hydrogen environment. The results show that the critical Mode-I stress intensity factor (SIF) is reduced due to the presence of hydrogen, but the existence of $\Sigma 5$ grain boundaries (GBs, with inclination angle ranging from 0 to $\pi/4$) almost not alter the critical Mode-I SIF for dislocation emission, compared with the single crystal cases. These findings suggest that further large-scale investigations should be conducted to study the influence of various microstructural factors, such as, the distance from the crack tip to GB and density of GB as well as the existence of other defects, e.g. voids and inclusions.

Keywords: Grain boundaries; Dislocations; Crack tip plasticity; Hydrogen embrittlement

1. Introduction

Hydrogen atoms in metals can severely decrease the ductility and load capacity, thus cause catastrophic failure of materials, which is usually termed as hydrogen embrittlement (HE) [1-9]. Up to now, the HE in metals is mainly discussed with some widely-accepted phenomenological mechanisms, e.g. the hydrogen-enhanced decohesion (HEDE) [10-14], hydrogen-enhanced localized plasticity (HELP) [4,5,15], hydrogen-enhanced and strain-induced vacancies [16] and hydrogen-assisted nanovoiding [17-21], among which the HELP mechanism allows one to study the interactions between the hydrogen and plasticity. In past decades, the validity of HELP mechanism has been verified by numerous experimental [22,23] and numerical studies [24-27]. Analogous to the surfactant theory in chemistry, Kirchheim [28-30] proposed the defect acting agents (defactants) theory, which has been used to explain the hydrogen-induced reduction of pop-in force observed in nanoindentation tests [31,32]. However, the detailed mechanisms for

* Email address: zhiliang.zhang@ntnu.no

dislocation/hydrogen interaction is still under debate. The kinetic Monte Carlo studies [33] demonstrate that the velocity of the $1/2[111]$ screw dislocation in bcc-Fe could be either increased or decreased depending on the loading stress, temperature and hydrogen concentration. Recent molecular dynamics simulations [34] also show that the effect of hydrogen content on the plastic deformation occurring in nanoindentation tests is strongly dependent on the loading rate. Thus, a more complex picture can be anticipated, if other factors at different time and length scales, such as loading patterns, specimen geometry and crystal imperfections etc., were considered.

As a key ingredient of crystal imperfections, the grain boundary (GB) has been shown to be able to significantly affect the fracture behavior [35-37]. Specifically, GBs play an important role on affecting the transport and segregation of H atoms and fracture patterns in annealed polycrystalline materials [38]. Seita et al. [39] found that the low- Σ ($\Sigma=1-29$) GBs in Ni-based superalloy can act as a weak point for crack initiation, at the same time show considerable resistance against hydrogen-induced crack propagation. Earlier experimental studies [37] also show that the susceptibility to intergranular HE in metallic materials can be remarkably reduced by applying the grain boundary engineering techniques, i.e. increasing the fraction of “special” GBs, which are less likely to be preferred sites for H segregation. Recent X-ray absorption tomography measurements [40] further demonstrated that the fraction of GBs with low-index planes, i.e. boundaries where at least one of the neighboring grains has a low Miller index facet – $\{001\}$, $\{011\}$ or $\{111\}$ along the GB plane, should be maximized to design HE-resistant materials via GB engineering. Systematical atomistic studies also show that [41] the presence of H atoms reduces the critical load required for dislocation emission from GBs. Although these studies might suggest that the GBs can induce the change of intergranular fracture behaviors under H environment, few studies are dedicated to understand the transgranular HE process. In order to shed more lights on the GB-related fracture process under H environment, here we performed a systematical set of atomistic simulations of the cracked Ni crystals to investigate the plasticity near the crack tip. As a representative type among the low- Σ GBs, without the loss of generality, the effect of $\Sigma 5$ GBs on the crack-tip plasticity is examined in present study.

2. Computational details

Atomistic simulations are performed by using the Large-scale Atomic/Molecular Massively Parallel Simulator (LAMMPS) open source code [42]. The pair interaction in Ni-H system is described using the embedded-atom method (EAM) potential tabulated by Angelo et al. [43]. According to the coincident site lattice theory, bicrystal specimens with a specified $\Sigma 5$ GB perpendicular to the crack plane are created by joining two separate single crystals together and deleting the overlapped atoms [44]. The information of inclination angle and boundary plane of six $\Sigma 5$ GBs can be found in **Table 1**. For reference, the cracked Ni single crystal model is also built, with the geometry details presented in **Table 2**. For the simulation of crack propagation, all the specimens are cut into the circular plate with the same radius (100 Å) and thickness (88 Å). The periodic boundary condition is applied along the crack front, i.e. the z-axis in Cartesian coordinates. The H atoms are inserted near the crack tip and GB by using the method described in [45], in which the H atoms are randomly inserted within a cylindrical region of radius 20 Å around the crack-tip at a

rate of 1 atom/ps. While for the GB segregation, a rectangular region of 40 Å with 20 Å wide in each side of the GB interface along the x -direction is defined to allow adding H atoms by using the similar procedure as putting H atoms into the cylindrical region around the crack tip. After inserting every 100 H atoms, the system is relaxed for 4 ns to allow the H segregation. Due to the fact that there exists locally high stress concentration around crack-tip and GB, it is reasonable to insert H atoms in these regions, as shown in [Fig. 1](#). An atomically blunt crack is introduced by removing several layers of atoms in the left side of the specimens. In order to get the results as general as possible, we designed specimens with 3 different crack-tip radius ($R = 2, 5$ and 8 Å) for each case shown in [Table 1](#) and [Table 2](#).

First shown by Irwin [\[46\]](#), there exist three basic modes of crack extension, i.e., the Mode-I (tensile opening), Mode-II (forward shearing) and Mode-III (longitudinal shearing) loadings, among which the Mode-I type occurs often and has been studied extensively. In the framework of linear-elastic fracture mechanics (LEFM), the stress field around the crack tip can be uniquely described by a parameter named as the stress intensity factor (SIF), with more details can be found in textbooks of fracture mechanics. Here, the Mode-I SIF K_I field [\[47,48\]](#) is applied on the boundary atoms according to the isotropic LEFM solution of displacement field around the crack tip,

$$u_x(r, \theta) = K_I \frac{1+\nu}{E} \sqrt{\frac{r}{2\pi}} \cos\left(\frac{\theta}{2}\right) \left(2 - 4\nu + 2\sin^2\frac{\theta}{2}\right) \quad (1)$$

$$u_y(r, \theta) = K_I \frac{1+\nu}{E} \sqrt{\frac{r}{2\pi}} \sin\left(\frac{\theta}{2}\right) \left(4 - 4\nu - 2\cos^2\frac{\theta}{2}\right) \quad (2)$$

where r is the distance between crack tip and the present position, θ is the angle between the crack plane and the direction of r , ν is Poisson's ratio, and E is Young's modulus. It should be noted that relatively small size specimen is used in this study, due to the limitation of computational resources. Zhu et al. [\[49\]](#) have studied the finite-size effects on the dislocation emission in fcc Cu, and found that the effect of simulation cell boundary on the transition state is expected to be much weaker than that on the final state, where the equilibrium location of a fully formed dislocation loop sensitively depends on the size of the simulation cell. Since the nucleation event is mainly controlled by the transition state, the effect of specimen size on the critical SIF required for dislocation nucleation is acceptable.

The system temperature is fixed at 300 K by using an isothermal-isobaric (NPT) ensemble with a Nosé-Hoover thermostat and barostat [\[50,51\]](#). Since the x - and y -directions are non-periodic, the constant pressure constraint is only applied along the z -direction. The equations of motion are integrated by a standard velocity-Verlet algorithm with a time-step of 1 fs. During the modelling, we calculate the common neighbor analysis [\[52,53\]](#) and centro-symmetry parameters [\[54\]](#) for post-processing. Dislocation tracking and identification are performed by means of the Dislocation eXtraction Algorithm (DXA) [\[55\]](#), which transforms the original atomistic representation of a dislocated crystal into a line-based representation of the dislocation networks, thus can determine the Burgers vector of each dislocation segment and identify dislocation junctions. The post-process visualization is mainly done by the OVITO software [\[56\]](#). The critical SIF upon the emission of dislocations is marked as the incipient event of plasticity observed by DXA algorithm [\[55\]](#).

Fig. 1. 3D schematic of the cracked model for MD simulations.

(a) without the presence of hydrogen, colored by the stress tensor component σ_{xx} (in the unit of bar); (b) with the presence of hydrogen (red color).

Table 1. Geometry of bicrystal specimens with six different $\Sigma 5$ GB characters.

ST represents symmetrical tilt, and AT is asymmetrical tilt. GB plane (hkl) L/R means the Miller index of GB in Left and Right side grain, respectively.

Specimen-#	GB type	Inclination angle ϕ	GB plane (hkl) L/R	Number of Ni-atoms
$\Sigma 5$ -GB1	ST	0	(310)/($\bar{3}$ 10)	253050
$\Sigma 5$ -GB2	AT	11.31	(740)/($\bar{8}$ 10)	253000
$\Sigma 5$ -GB3	AT	18.43	(430)/(100)	253150
$\Sigma 5$ -GB4	AT	26.57	(110)/(710)	253500
$\Sigma 5$ -GB5	AT	30.96	(670)/(920)	253050
$\Sigma 5$ -GB6	ST	45	(210)/(120)	253175

Table 2. Geometry of single crystal specimens with six different orientations, which are the same as the left side grain in bicrystals respectively. The z-axis of all specimens is along $[00\bar{1}]$ direction.

Specimen-#	Cartesian x-axis	Cartesian y-axis	Ni-atom numbers
Ni-SC1	[310]	[1 $\bar{3}$ 0]	243225
Ni-SC2	[740]	[4 $\bar{7}$ 0]	282825
Ni-SC3	[430]	[3 $\bar{4}$ 0]	297825
Ni-SC4	[110]	[1 $\bar{1}$ 0]	304175
Ni-SC5	[670]	[7 $\bar{6}$ 0]	302325
Ni-SC6	[120]	[2 $\bar{1}$ 0]	273025

3. Results and discussions

3.1 Crack-tip plasticity in Ni specimens without the presence of hydrogen

In order to understand the effect of GBs on the crack-tip plasticity under H environment, in this section, we firstly present the MD results of the complex crack-tip behaviors (see [Appendix](#) for the definition) in both single crystals and bicrystals without the presence of hydrogen. In [Fig. 2](#), the typical process of semi-brittle and ductile blunt events in Ni-SC4 specimens with two different tip radius ($R = 2 \text{ \AA}$ and 8 \AA) are presented. As shown in [Fig. 2\(a-d\)](#), at $K_I = 1.23 \text{ MPa}\sqrt{\text{m}}$, a new sharp tip is formed together with the nucleation of Shockley partial dislocations ($R = 2 \text{ \AA}$), and

promotes the crack propagation accompanied with the formation of stair-rod dislocations at $K_I = 1.45 \text{ MPa}\sqrt{\text{m}}$. For the ductile blunt process in the specimen with a tip radius of 8 \AA shown in **Fig. 2(e-h)**, crack front almost does not move in the whole loading process. Compared with the one with a sharper tip, where the dislocations activity is mainly localized around the crack tip, the stacking fault ribbons (marked as red atoms) can extend to the whole space inside the specimen here with a blunter tip. The above observations can be summarized as that, the $1/6\langle 211 \rangle$ Shockley partial will be nucleated firstly, while the dislocation behavior would be more active in a specimen with larger tip radius.

Fig. 2. Typical snapshots of fracture behavior in single crystal specimens without H charged.

(a-d) *semi-brittle* events in Ni-SC4 single crystal specimen with a tip radius $R = 2 \text{ \AA}$; (e-h) *ductile blunt* events in Ni-SC4 specimen with a tip radius $R = 8 \text{ \AA}$. The atoms are colored by DXA analysis, with blue as fcc, red as hcp, green as bcc and white as unknown type. All the specimens are partly sliced along the z -axis to show the dislocation lines, for which the green color represents $1/6[112]$ Shockley partial, purple as $1/6[110]$ stair-rod, and yellow as $1/3[111]$ Hirth dislocation, respectively.

In order to explore the effect of GB on the fracture behavior in fcc Ni specimens, we analyze the fracture process of the corresponding $\Sigma 5$ -GB4 specimens with two different tip radius ($R = 2 \text{ \AA}$ and 8 \AA) in **Fig. 3**. For the specimen with a crack-tip radius of $R = 2 \text{ \AA}$ as shown in **Fig. 3(a-d)**, at $K_I = 1.24 \text{ MPa}\sqrt{\text{m}}$, the crack-tip advances with dislocation emission simultaneously. With continuous loading, dislocations are emitted, reach the GB, and cannot transport into the right side grain until $K_I = 1.53 \text{ MPa}\sqrt{\text{m}}$. The typical process of ductile blunting in a $\Sigma 5$ -GB4 specimen ($R = 8 \text{ \AA}$) can be seen in **Fig. 3(e-h)**. The snapshots show that the crack front will not move, while the crack-tip deformation is relieved by the rearrangement of atoms. At $K_I = 1.35 \text{ MPa}\sqrt{\text{m}}$, the stacking fault is already emitted from the crack front, and transmits to the GB. The results show that the evolution of microstructures seems not to be affected by the tip radius.

Fig. 3. Typical snapshots of fracture behavior in bicrystal specimens without H charged.

(a-d) *semi-brittle* events in $\Sigma 5$ -GB4 specimen with a tip radius $R = 2 \text{ \AA}$; (e-h) *ductile blunt* events in $\Sigma 5$ -GB4 specimen with a tip radius $R = 8 \text{ \AA}$. The atoms are colored by DXA analysis, with blue as fcc, red as hcp, green as bcc and white as unknown type. All the specimens are partly sliced along the z -axis to show the dislocation lines, for which the green color represents $1/6[112]$ Shockley partial, purple as $1/6[110]$ stair-rod, and yellow as $1/3[111]$ Hirth dislocation, respectively.

3.2 Crack-tip plasticity in Ni specimens with the presence of hydrogen

Fig. 4 shows the development of crack-tip behaviors in single crystal specimens with two different tip radius ($R = 2 \text{ \AA}$ and 8 \AA) under H environment. As shown in **Fig. 4(a-d)**, in the specimen with a tip radius $R = 2 \text{ \AA}$, the dislocation

emission is already observed at $K_I = 1.23 \text{ MPa}\sqrt{\text{m}}$, and a stacking fault ribbon is emitted from the crack surface at $K_I = 1.35 \text{ MPa}\sqrt{\text{m}}$. The specimen with a tip radius $R = 8 \text{ \AA}$ shows a similar process, but stacking fault is already formed at $K_I = 1.23 \text{ MPa}\sqrt{\text{m}}$ in **Fig. 4(e)**. **Fig. 5** displays the evolution of ductile blunt event in bicrystal specimens with two different tip radius ($R = 2 \text{ \AA}$ and 8 \AA) under H environment. As can be seen in **Fig. 5(a)**, in the specimen with a tip radius $R = 2 \text{ \AA}$, the stacking fault is formed earlier than in the single crystal specimen. Similar evolution is observed for the specimen with a tip radius $R = 8 \text{ \AA}$ shown in **Fig. 5(e-h)**, but the dislocation is much easier to be activated. Compared with the specimens without the presence of hydrogen shown in **Fig. 2** and **Fig. 3**, the insertion of hydrogen atoms causes severe distortion of lattice structure and promote the dislocation formation. Previous studies of nickel-based alloy [57,58] have demonstrated that the characteristic plasticity via dislocation process would be enhanced by the presence of hydrogen. The present result also suggests that the slip planarity is not affected by H atoms, thus is consistent with the recent experiments [58].

Fig. 4. Snapshots of *ductile blunt* events in Ni-SC4 specimen under H environment (with 200 H atoms charged around crack-tip).

(a-d) with a tip radius $R = 2 \text{ \AA}$; (e-h) with a tip radius $R = 8 \text{ \AA}$. The atoms are colored by DXA analysis, with blue as fcc, red as hcp, green as bcc and white as unknown type. All the specimens are partly sliced along the z -axis to show the dislocation lines, for which the green color represents $1/6[112]$ Shockley partial, purple as $1/6[110]$ stair-rod, and yellow as $1/3[111]$ Hirth dislocation, respectively.

Fig. 5. Snapshots of *ductile blunt* events in $\Sigma 5$ -GB4 specimen under H environment (with 200 H atoms charged around crack-tip).

(a-d) with a tip radius $R = 2 \text{ \AA}$; (e-h) with a tip radius $R = 8 \text{ \AA}$. The atoms are colored by DXA analysis, with blue as fcc, red as hcp, green as bcc and white as unknown type. All the specimens are partly sliced along the z -axis to show the dislocation lines, for which the green color represents $1/6[112]$ Shockley partial, purple as $1/6[110]$ stair-rod, and yellow as $1/3[111]$ Hirth dislocation, respectively.

Furthermore, the measurement of dislocation density shown in **Fig. 6** clearly demonstrates that, i) the insertion of H atoms would increase the dislocation density, compared with the specimens without H charged for both single crystal (see **Fig. 6(a)**) and bicrystal (**Fig. 6(b)**) scenarios; ii) the existence of GB seems not to induce significant influence on the evolution of dislocation density. In order to gain a general understanding of dislocation emission under hydrogen environment, we summarize the statistical distribution of critical K_{Ie} values obtained from all the MD simulations as a function of local hydrogen concentration in **Fig. 7**. It is found that the mean value of K_{Ie} for both bicrystal (single crystal) specimens decreases from ~ 1.28 (1.15) $\text{MPa}\sqrt{\text{m}}$ to 1.12 (1.10) $\text{MPa}\sqrt{\text{m}}$ when hydrogen atoms are inserted near the crack tip. This finding is similar to the study of the intergranular fracture in Ni specimens [41], thus supports the application of the HELP model at atomic scale. Comparing the data of **Fig. 7(a)** and **(e)**, we found that the existence of GBs almost does not change the lower bound, but slightly elevates the upper bound of the distribution of the critical SIF required for dislocation emission at lower H concentration (i.e. more data points are located in the region larger than $1.2 \text{ MPa}\sqrt{\text{m}}$). These results thus indicate that in the practical experiments with polycrystalline Ni, the variation

of HE resistance induced by $\Sigma 5$ GBs is not significant in present simulation settings. However, the distance from the tip to GB as well as inclination angles and density of GB might influence the results, and should be investigated in future studies. Specifically, by comparing the results shown in Fig. 7(b-d) and (f-h), we found that the slight increase of average value of K_{Ic} in bicrystal is mainly contributed by the specimens with crack tip radius $R = 2 \text{ \AA}$, while for the other tip geometries the K_{Ic} is almost not affected by the GBs. It should be noted that the increasing of K_{Ic} may prompt the cleavage mode in Rice model. Thus, this conclusion has to be limited to the scenario studied here, while in the practical experiments larger proportion of GBs will lead to the fact that nano-grain materials are more brittle than the coarse-grain ones since it is easier for the intergranular fracture to occur. Besides, the statistical analysis also demonstrates that the K_{Ic} value almost does not vary with hydrogen concentration. This finding is consistent with our previous study [34] about the nanoindentation tests under hydrogen environment, where the pop-in load is also not sensitive to the hydrogen content. The reason could be that under high loading rates, the hydrogen could not interact with the newly formed dislocations immediately. In laboratory experiments, since lower loading rates allow the formation of Cottrell atmosphere around dislocations, the continuous decreasing of K_{Ic} with increasing H concentration can be expected.

Fig. 6. The evolution of dislocation density in the specimens corresponding to Fig. 2-5.

(a) Ni-SC4 specimen without H charged, corresponding to Fig. 2, and with 200 H atoms located around the crack tip, corresponding to Fig. 4; (b) $\Sigma 5$ -GB4 specimen without H charged, corresponding to Fig. 3, and with 200 H atoms located around the crack tip, corresponding to Fig. 5. The black and blue lines represent the specimen with a tip radius $R = 2 \text{ \AA}$, while the red and green ones for $R = 8 \text{ \AA}$.

Fig. 7. Statistical distributions of the MD results of the critical Mode I stress intensity factor K_{Ic} v.s. the number of H atoms inserted in the vicinity of crack-tip.

(a-d) for bicrystal Ni: (a) is the total distribution for all bicrystal specimens with 3 different tip radius, while (b) is for $R = 2 \text{ \AA}$ specimens, (c) is for $R = 5 \text{ \AA}$ specimens, and (d) is for $R = 8 \text{ \AA}$ specimens; (e-h) for single-crystal Ni: (e) is the total distribution for all single crystal specimens with 3 different tip radius, while (f) is for $R = 2 \text{ \AA}$ specimens, (g) is for $R = 5 \text{ \AA}$ specimens, and (h) is for $R = 8 \text{ \AA}$ specimens. Each solid line represents a normal distribution of K_{Ic} (i.e. the open symbols) for specimens that show ductile blunt or semi-brittle features.

4. Concluding remarks

We report the MD simulations of the crack-tip plasticity under hydrogen environment. The simulation results show that the critical SIF K_{Ic} required for dislocation emission is reduced in the specimens with the presence of hydrogen, thus support the validation of HELP mechanism at nanoscale. However, the K_{Ic} seems not to be sensitive with the variation of hydrogen content, since the hydrogen could not interact with the newly formed dislocation immediately under high loading rates. Compared with single crystal specimens, the existence of $\Sigma 5$ GBs with different inclination angles almost does not change the K_{Ic} , thus does not significantly affect the fracture behavior under high loading rates.

These results might suggest that the intragranular fracture is not favored in HE of metals, thus support the previous experimental findings [22,40,59-63], where the H-assisted fracture is usually intergranular. However, HE cannot be attributed to one simple mechanism, but is rather a collective result of H interactions with microstructures distributed on length-scales differing by orders of magnitude. Therefore, further studies should be focused on the influence of various microstructural factors, such as, the distance from the crack tip to GB and density of GB as well as the existence of other defects, e.g. voids [19-21] and inclusions [64-66].

Appendix

As shown in Fig. A1, depending on the crystallographic orientation and crack-tip geometry, three typical crack-tip events namely, brittle cleavage, ductile blunt and semi-brittle are observed in all MD simulations of single crystal and bicrystal specimens. Here the brittle cleavage is defined as the sharp crack propagation without dislocation emission, while the new-formed cleavage plane is not necessarily parallel with the original crack plane. The ductile blunt is defined as the event that Shockley partial is emitted at the same time the crack front does not move, and the semi-brittle event means that dislocation emission and crack propagation are activated simultaneously.

Fig. A1. Three typical events observed in all MD simulations in present study.

Brittle cleavage is defined as the crack propagation without dislocation emission, while ductile blunt is the event that the crack-tip is blunted by dislocation emission, and semi-brittle means the crack propagation accompanied with dislocation emission simultaneously. The atoms are colored by adaptive common neighbor analysis, with blue as bcc, cyan as hcp, green as fcc and red as unknown type.

Acknowledgements

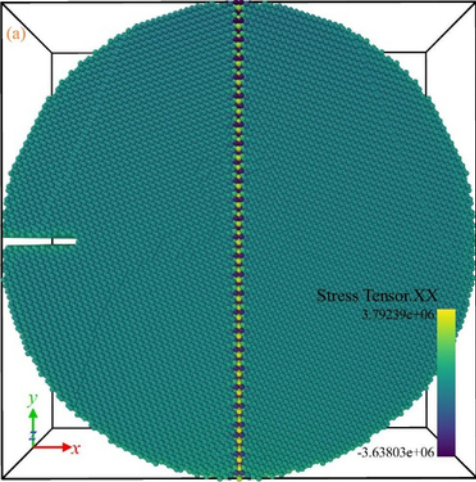
K.Z. acknowledges the constructive discussions with Prof. Alexander Hartmaier, Prof. William A. Curtin and Dr. Inga Gudem Ringdalen. Financial support for this work is provided by the Research Council of Norway under the “Hydrogen-induced degradation of offshore steels in aging infrastructures - models for prevention and prediction (HIPP)” project (No. 234130/E30). All simulations are carried out on the NOTUR (Grant No. NN9110K, NN9391K) high performance computer clusters Vilje at NTNU, Trondheim and Stallo at UiT, Tromsø.

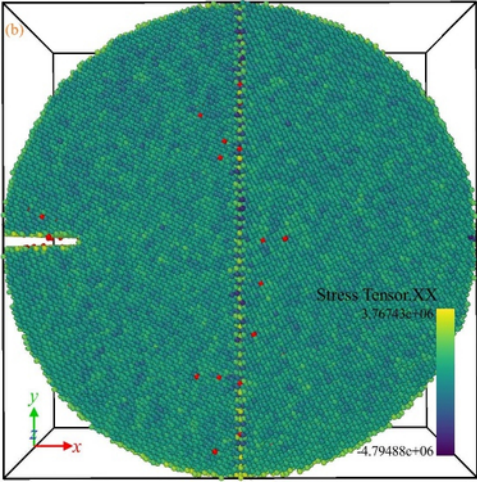
References

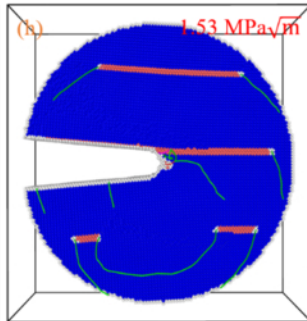
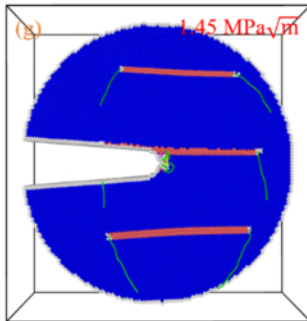
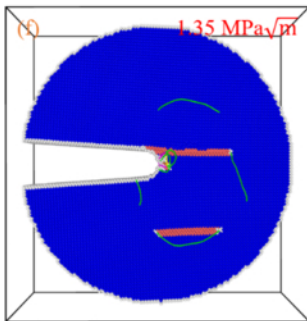
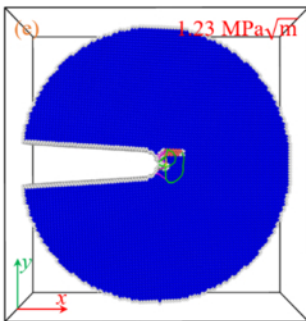
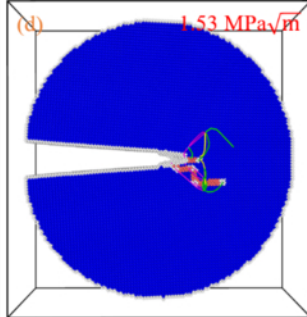
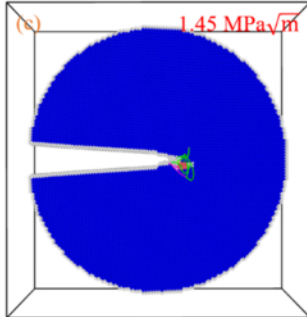
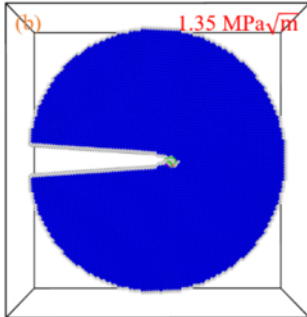
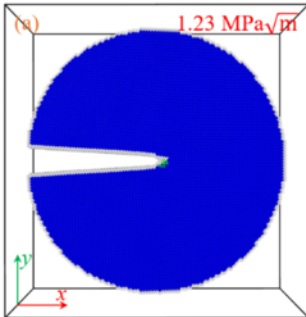
- [1] O. Barrera *et al.*, *J. Mater. Sci.* **53**, 6251 (2018).
- [2] S. K. Dwivedi and M. Vishwakarma, *Int. J. Hydrog. Energy* **43**, 21603 (2018).
- [3] R. A. Oriani, *Annu. Rev. Mater. Sci.* **8**, 327 (1978).

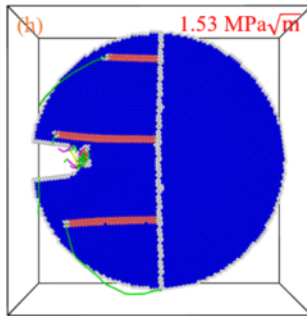
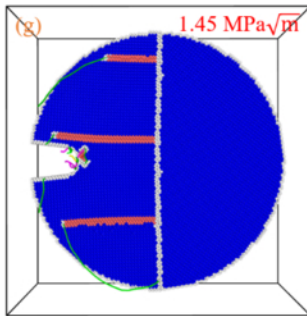
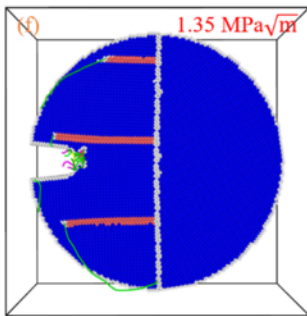
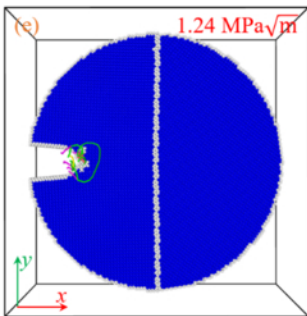
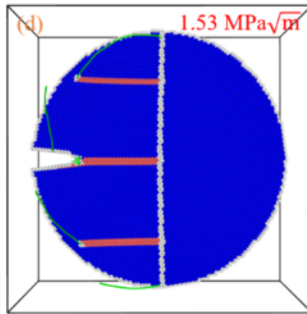
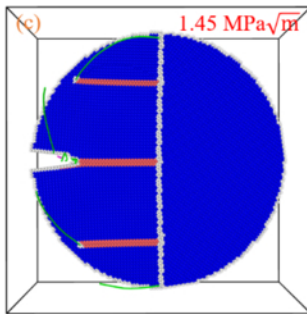
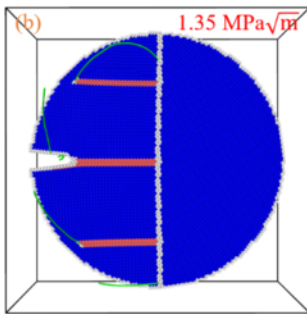
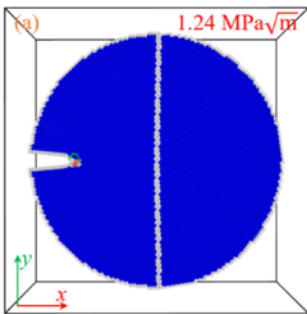
- [4] H. K. Birnbaum and P. Sofronis, *Mater. Sci. Eng. A* **176**, 191 (1994).
- [5] I. M. Robertson, *Eng. Fract. Mech.* **68**, 671 (2001).
- [6] I. M. Robertson, P. Sofronis, A. Nagao, M. L. Martin, S. Wang, D. W. Gross, and K. E. Nygren, *Metall. Mater. Trans. B* **46**, 1085 (2015).
- [7] M. Dadfarnia, P. Novak, D. C. Ahn, J. B. Liu, P. Sofronis, D. D. Johnson, and I. M. Robertson, *Adv. Mater.* **22**, 1128 (2010).
- [8] P. Cotterill, *Prog. Mater. Sci.* **9**, 205 (1961).
- [9] M. R. Louthan, D. E. Rawl, G. R. Caskey, and J. A. Donovan, *Mater. Sci. Eng.* **10**, 357 (1972).
- [10] R. A. Oriani, *Annu. Rev. Mater. Sci.* **8**, 327 (1978).
- [11] A. R. Troiano, *Trans. Am. Soc. Met.* **52**, 54 (1960).
- [12] W. W. Gerberich, R. A. Oriani, M. J. Lji, X. Chen, and T. Foecke, *Philos. Mag. A* **63**, 363 (1991).
- [13] R. A. Oriani and P. H. Josephic, *Acta Metall.* **22**, 1065 (1974).
- [14] E. A. Steigerwald, F. W. Schaller, and A. R. Troiano, *Trans. Metall. Soc. AIME* **218**, 832 (1960).
- [15] C. D. Beachem, *Metall. Trans.* **3**, 441 (1972).
- [16] M. Nagumo, *Mater. Sci. Technol.* **20**, 940 (2004).
- [17] S. Li *et al.*, *Int. J. Plast.* **74**, 175 (2015).
- [18] T. Neeraj, R. Srinivasan, and J. Li, *Acta Mater.* **60**, 5160 (2012).
- [19] K. Zhao, J. Y. He, I. G. Ringdalen, and Z. L. Zhang, *J. Appl. Phys.* **123**, 245101 (2018).
- [20] M. Q. Chandler, M. F. Horstemeyer, M. I. Baskes, G. J. Wagner, P. M. Gullett, and B. Jelinek, *Acta Mater.* **56**, 619 (2008).
- [21] M. Q. Chandler, M. F. Horstemeyer, M. I. Baskes, P. M. Gullett, G. J. Wagner, and B. Jelinek, *Acta Mater.* **56**, 95 (2008).
- [22] M. L. Martin, B. P. Somerday, R. O. Ritchie, P. Sofronis, and I. M. Robertson, *Acta Mater.* **60**, 2739 (2012).
- [23] M. L. Martin, J. A. Fenske, G. S. Liu, P. Sofronis, and I. M. Robertson, *Acta Mater.* **59**, 1601 (2011).
- [24] P. Sofronis and H. K. Birnbaum, *J. Mech. Phys. Solids* **43**, 49 (1995).
- [25] D. C. Ahn, P. Sofronis, and R. H. Dodds, *Int. J. Hydrog. Energy* **32**, 3734 (2007).
- [26] H. Y. Yu, A. Cocks, and E. Tarleton, *J. Mech. Phys. Solids* **123**, 41 (2019).
- [27] Y. J. Gu and J. A. El-Awady, *J. Mech. Phys. Solids* **112**, 491 (2018).
- [28] R. Kirchheim, *Scripta Mater.* **62**, 67 (2010).
- [29] R. Kirchheim, *Acta Mater.* **55**, 5129 (2007).
- [30] R. Kirchheim, *Acta Mater.* **55**, 5139 (2007).
- [31] A. Barnoush and H. Vehoff, *Acta Mater.* **58**, 5274 (2010).
- [32] A. Barnoush, N. Kheradmand, and T. Hajilou, *Scripta Mater.* **108**, 76 (2015).
- [33] I. H. Katzarov, D. L. Pashov, and A. T. Paxton, *Phys. Rev. Mater.* **1**, 033602 (2017).
- [34] K. Zhao, J. Y. He, A. E. Mayer, and Z. L. Zhang, *Acta Mater.* **148**, 18 (2018).
- [35] M. Kumar and C. A. Schuh, *Scripta Mater.* **54**, 961 (2006).
- [36] V. Randle, *Acta Mater.* **52**, 4067 (2004).
- [37] S. Bechtle, M. Kumar, B. P. Somerday, M. E. Launey, and R. O. Ritchie, *Acta Mater.* **57**, 4148 (2009).
- [38] D. H. Lassila and H. K. Birnbaum, *Acta Metall.* **34**, 1237 (1986).
- [39] M. Seita, J. P. Hanson, S. Gradecak, and M. J. Demkowicz, *Nat. Commun.* **6**, 6164 (2015).
- [40] J. P. Hanson, A. Bagri, J. Lind, P. Kenesei, R. M. Suter, S. Gradecak, and M. J. Demkowicz, *Nat. Commun.* **9**, 3386 (2018).
- [41] A. Tehrani and W. A. Curtin, *J. Mech. Phys. Solids* **101**, 150 (2017).
- [42] S. Plimpton, *J. Comput. Phys.* **117**, 1 (1995).
- [43] J. E. Angelo, N. R. Moody, and M. I. Baskes, *Modell. Simul. Mater. Sci. Eng.* **3**, 289 (1995).
- [44] L. Zhang, C. Lu, and K. Tieu, *Sci. Rep.* **4**, 5919, 5919 (2014).
- [45] J. Song and W. A. Curtin, *Nat. Mater.* **12**, 145 (2013).
- [46] G. R. Irwin, *J. Appl. Mech.* **24**, 361 (1957).
- [47] I. Ringdalen Vatne, A. Stukowski, C. Thaulow, E. Østby, and J. Marian, *Mater. Sci. Eng. A* **560**, 306 (2013).
- [48] I. Adlakha and K. N. Solanki, *J. Appl. Phys.* **123**, 014304 (2018).
- [49] T. Zhu, J. Li, and S. Yip, *Phys. Rev. Lett.* **93**, 025503 (2004).
- [50] W. G. Hoover, *Phys. Rev. A* **31**, 1695 (1985).
- [51] S. Nosé, *J. Chem. Phys.* **81**, 511 (1984).
- [52] H. Tsuzuki, P. S. Branicio, and J. P. Rino, *Comput. Phys. Commun.* **177**, 518 (2007).
- [53] D. Faken and H. Jónsson, *Comp. Mater. Sci.* **2**, 279 (1994).
- [54] C. L. Kelchner, S. J. Plimpton, and J. C. Hamilton, *Phys. Rev. B* **58**, 11085 (1998).

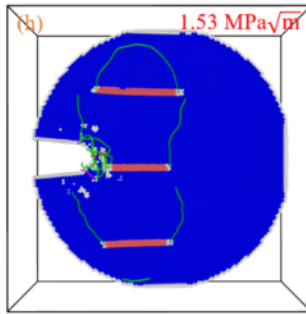
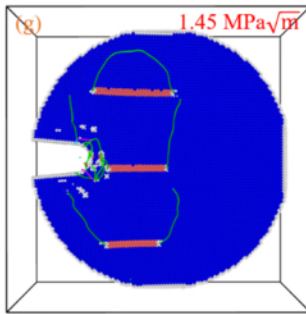
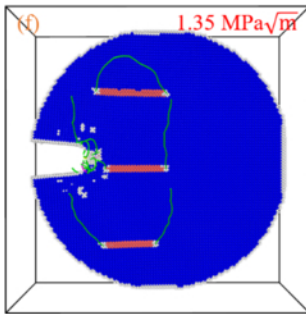
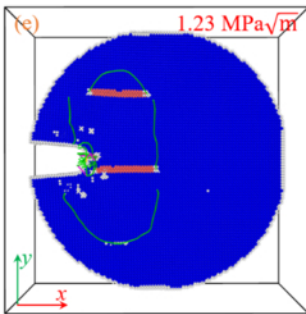
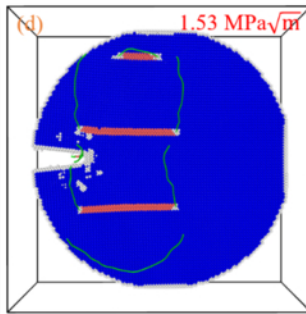
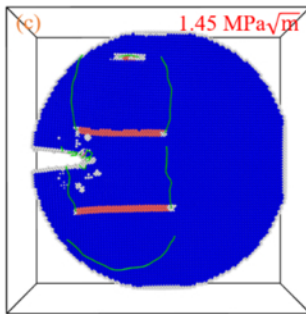
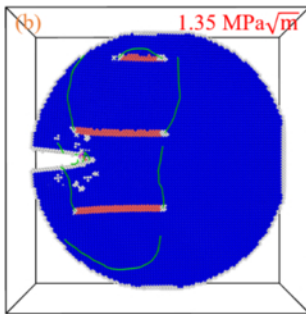
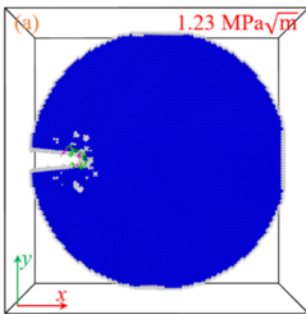
- [55] A. Stukowski, V. V. Bulatov, and A. Arsenlis, *Modell. Simul. Mater. Sci. Eng.* **20**, 085007 (2012).
- [56] A. Stukowski, *Modell. Simul. Mater. Sci. Eng.* **18**, 015012 (2010).
- [57] Z. B. Zhang, G. Obasi, R. Morana, and M. Preuss, *Acta Mater.* **113**, 272 (2016).
- [58] Z. B. Zhang, G. Obasi, R. Morana, and M. Preuss, *Scripta Mater.* **140**, 40 (2017).
- [59] E. Pouillier, A. F. Gourgues, D. Tanguy, and E. P. Busso, *Int. J. Plast.* **34**, 139 (2012).
- [60] S. K. Lawrence, B. P. Somerday, N. R. Moody, and D. F. Bahr, *JOM* **66**, 1383 (2014).
- [61] S. Wang, M. L. Martin, P. Sofronis, S. Ohnuki, N. Hashimoto, and I. M. Robertson, *Acta Mater.* **69**, 275 (2014).
- [62] C. A. Calhoun, E. Garlea, T. Sisneros, and S. R. Agnew, *J. Nucl. Mater.* **465**, 737 (2015).
- [63] R. M. Latanision and H. Opperhauser, *Metall. Trans.* **5**, 483 (1974).
- [64] W. Qin and J. A. Szpunar, *Philos. Mag.* **97**, 3296 (2017).
- [65] Z. B. Zhang, K. L. Moore, G. McMahon, R. Morana, and M. Preuss, *Corros. Sci.* **146**, 58 (2019).
- [66] R. Fratesi, G. Roventi, and M. Cavallini, *Mater. Sci. Eng. A* **119**, 17 (1989).

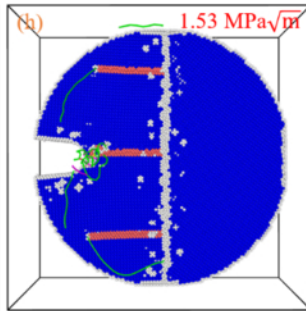
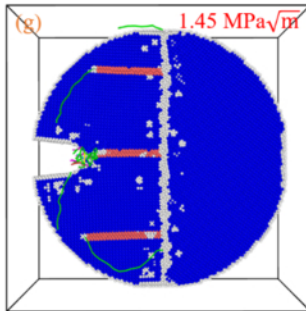
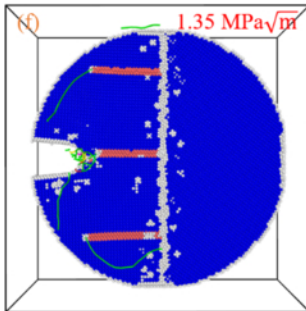
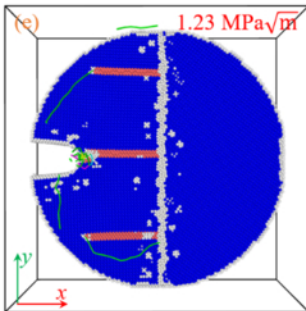
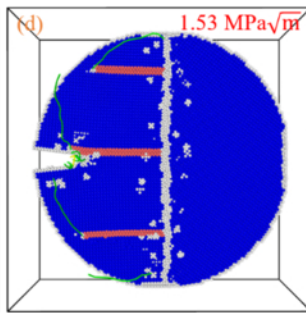
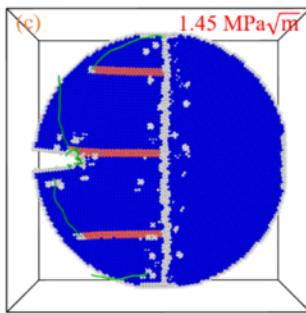
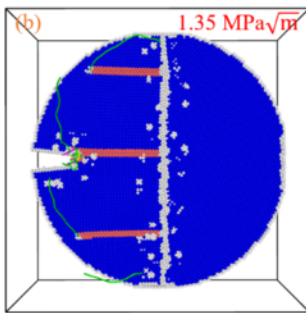
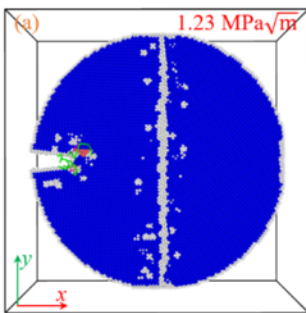


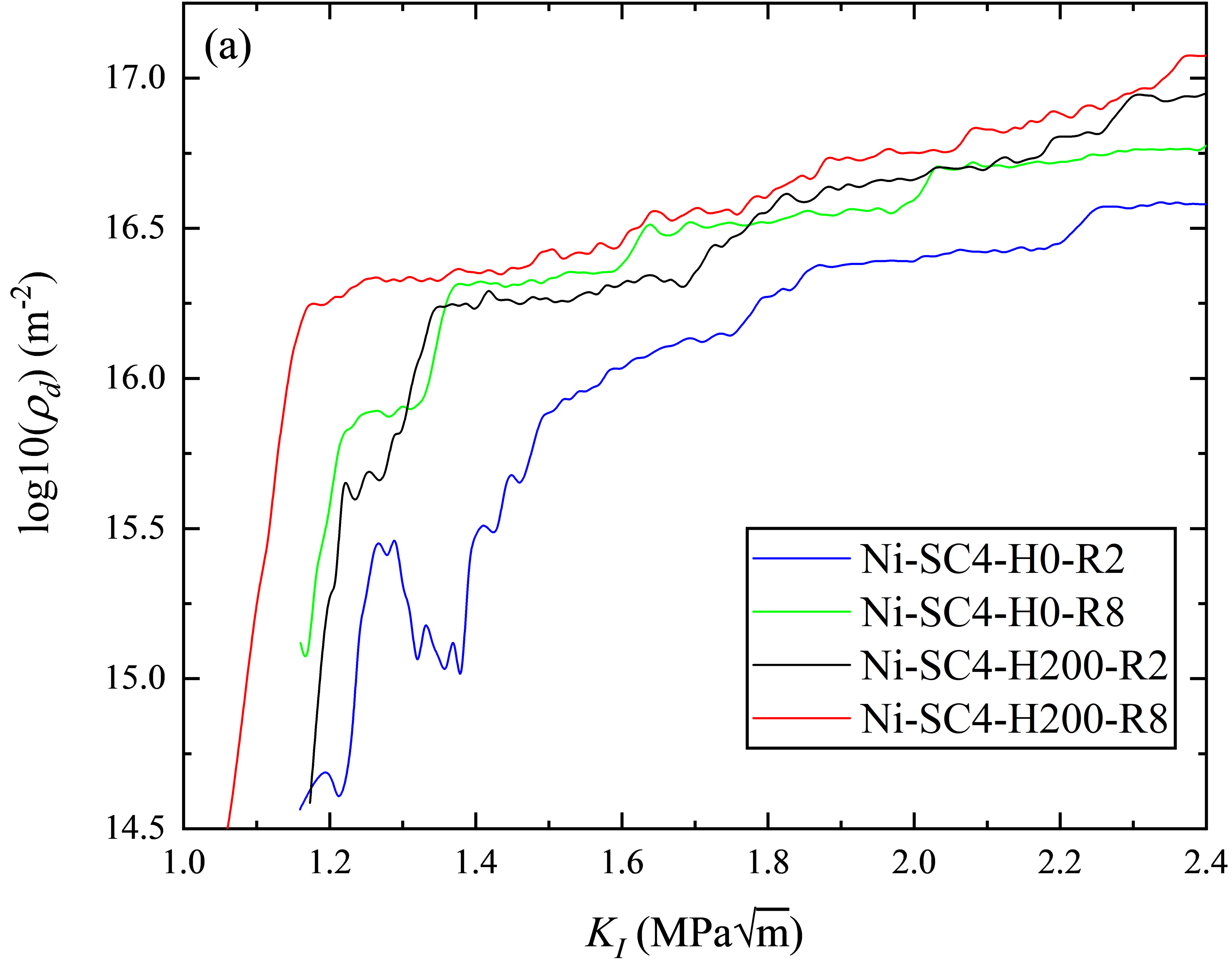


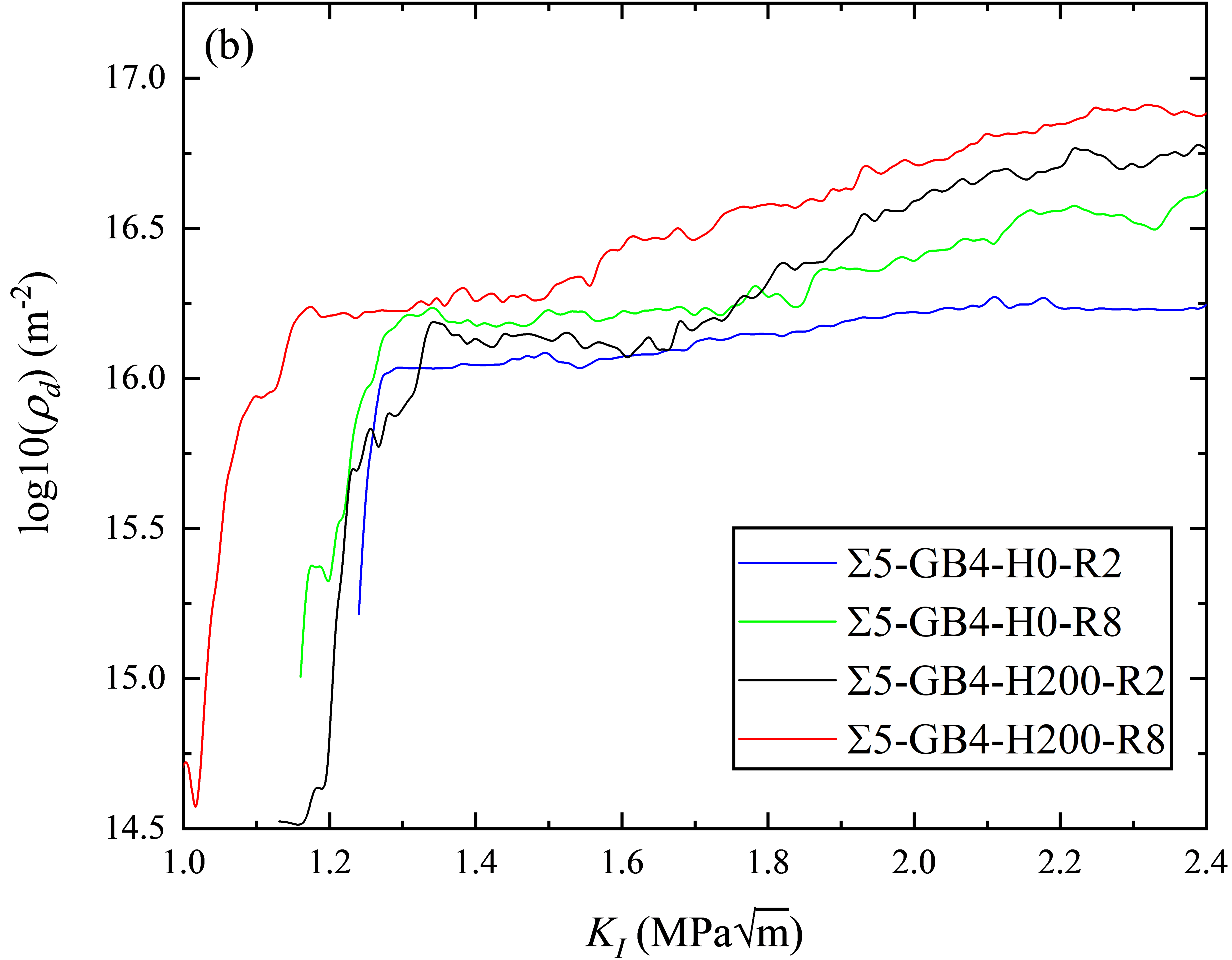












(a) bicrystal

K_{Ie} (MPa \sqrt{m})

1.5
1.4
1.3
1.2
1.1
1.0
0.9

0

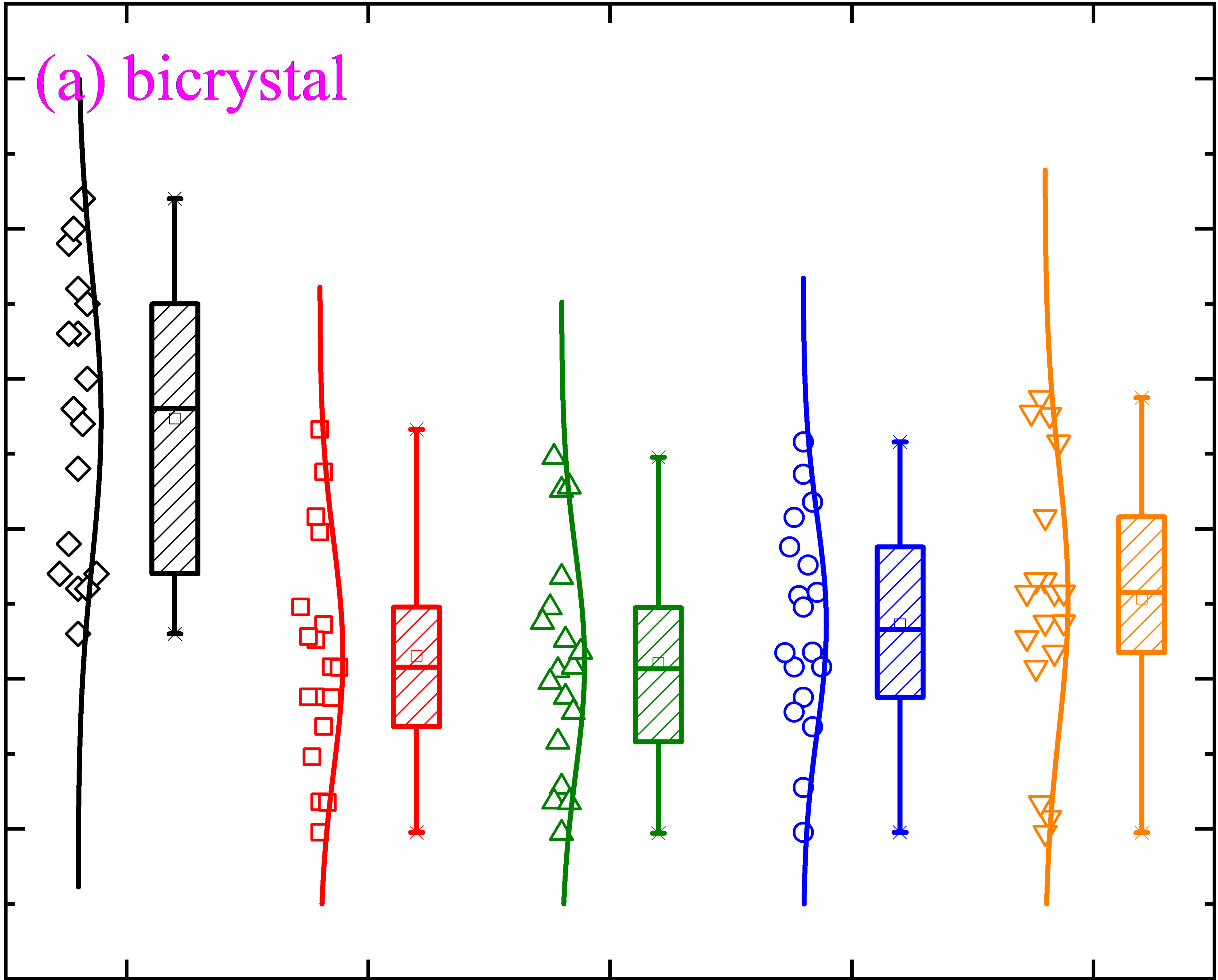
100

200

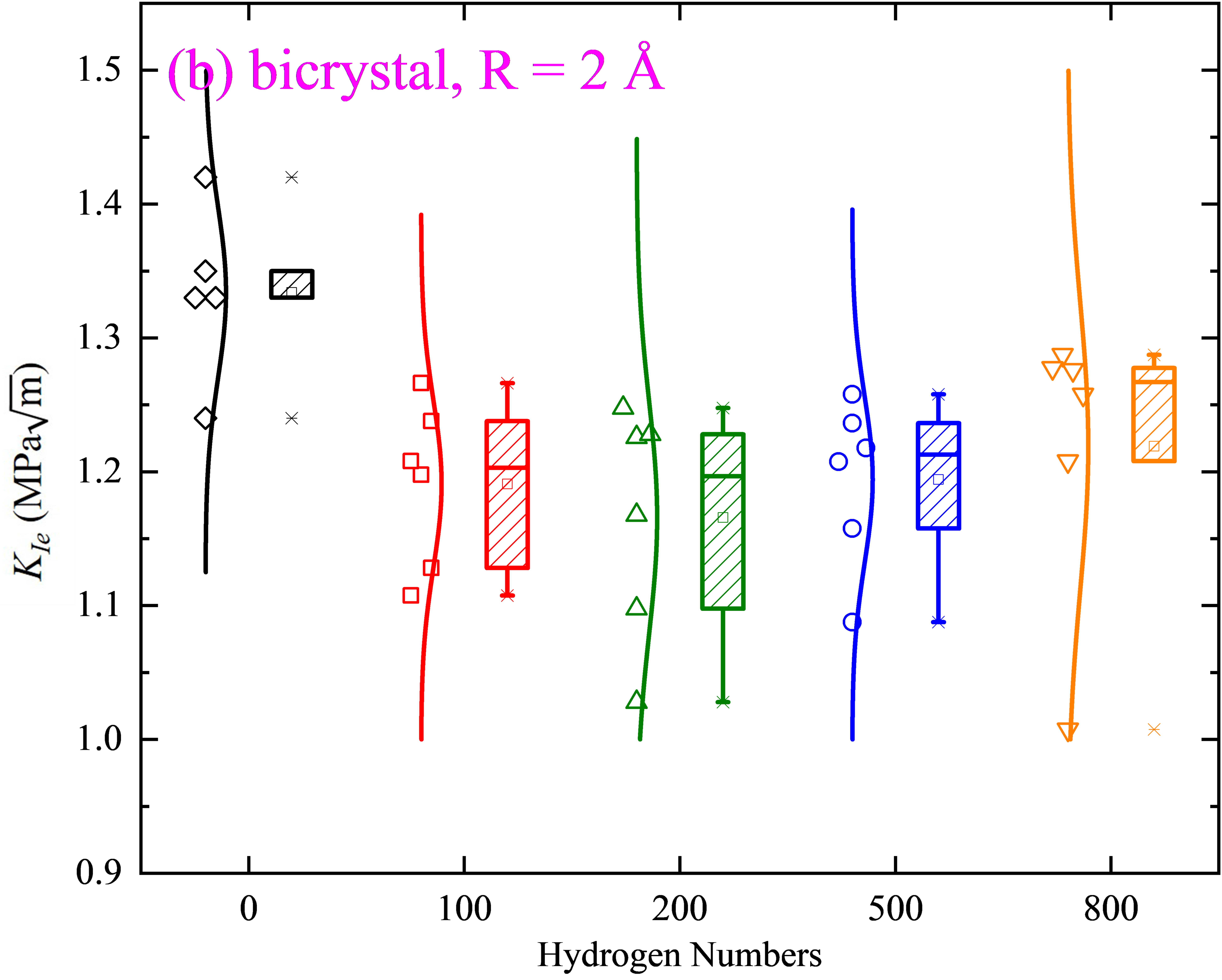
500

800

Hydrogen Numbers



(b) bicrystal, $R = 2 \text{ \AA}$



(c) bicrystal, $R = 5 \text{ \AA}$

$K_{Ie} \text{ (MPa}\sqrt{\text{m}})$

1.5
1.4
1.3
1.2
1.1
1.0
0.9

0

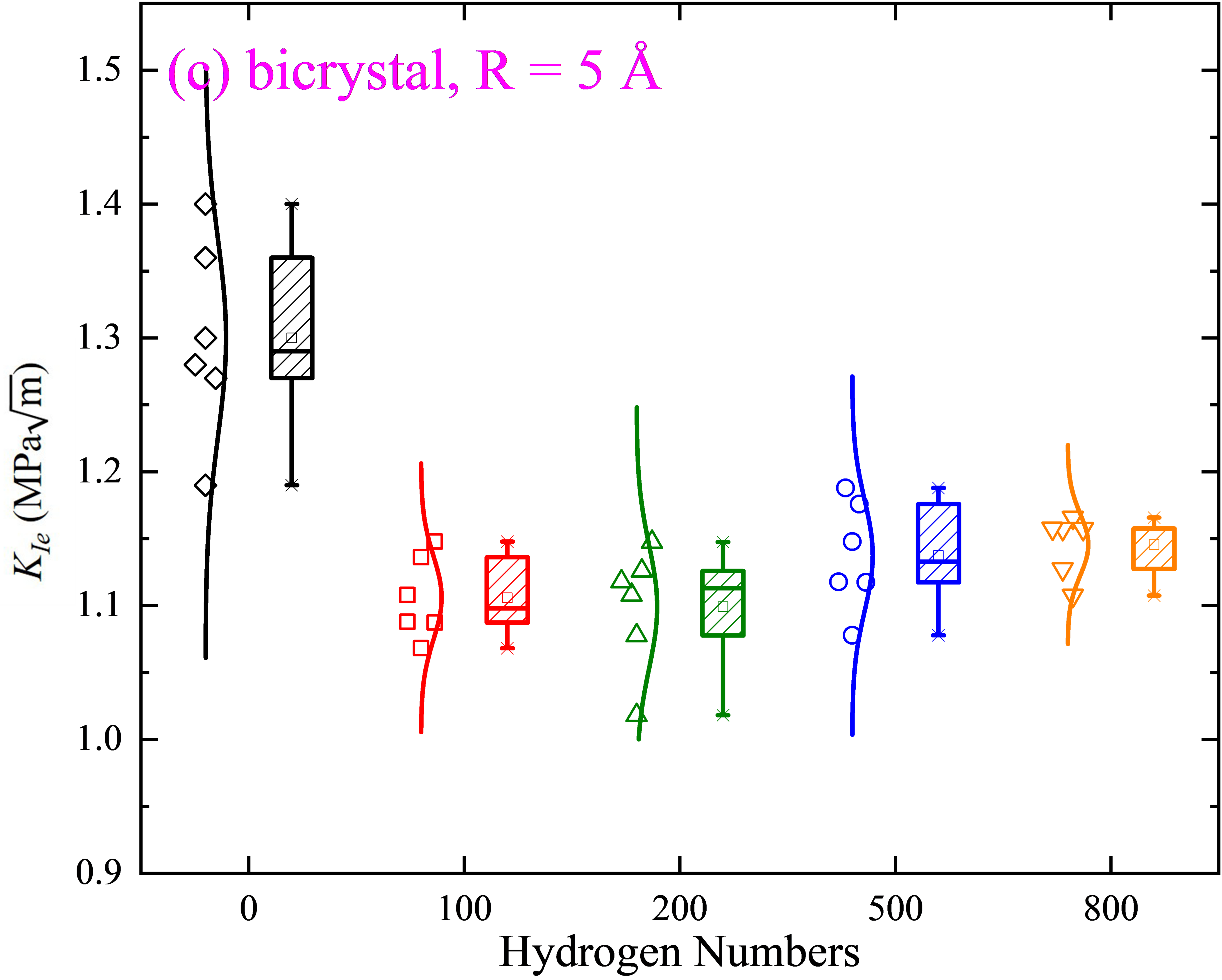
100

200

500

800

Hydrogen Numbers



(d) bicrystal, $R = 8 \text{ \AA}$

K_{Ie} (MPa $\sqrt{\text{m}}$)

1.5
1.4
1.3
1.2
1.1
1.0
0.9

0

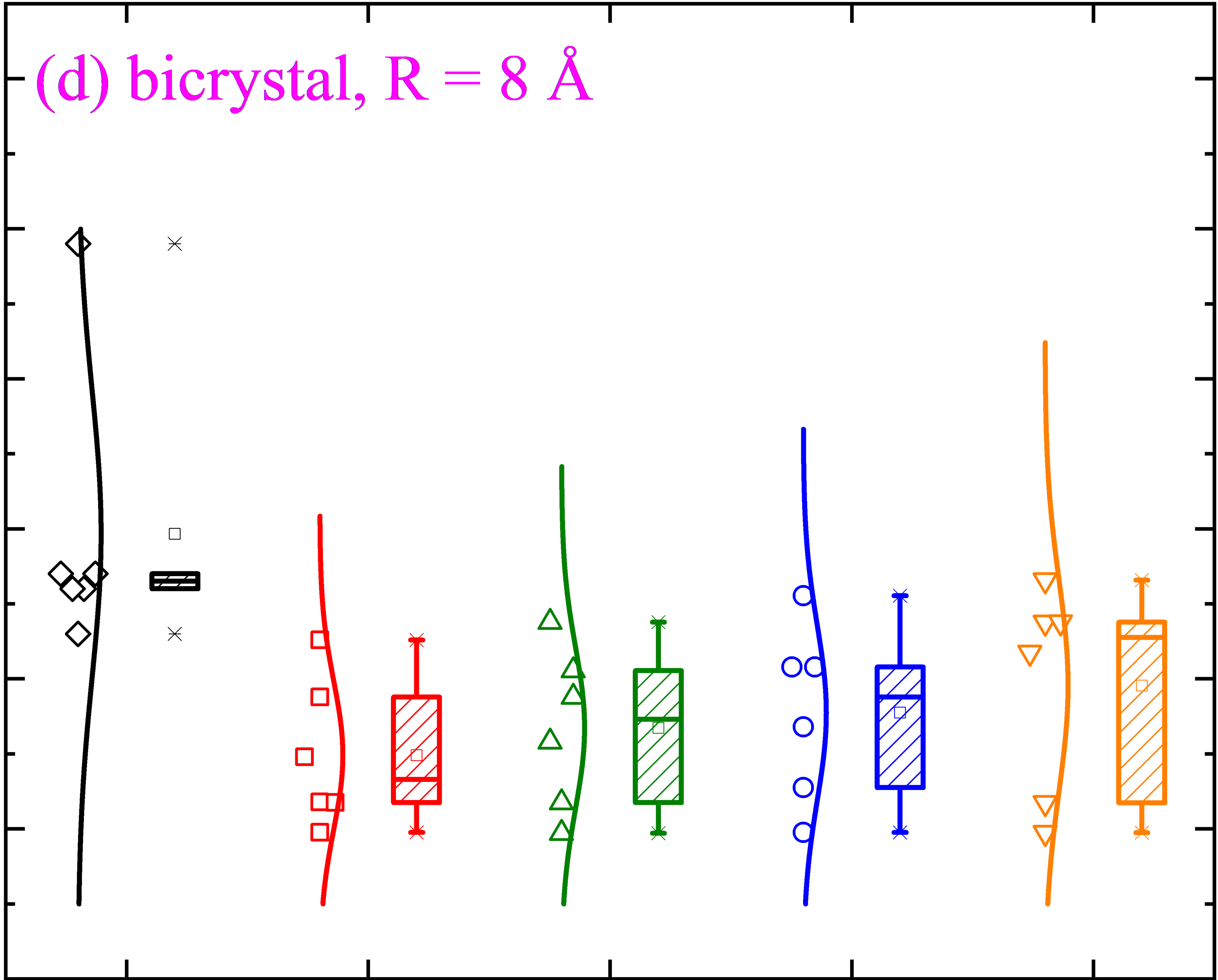
100

200

500

800

Hydrogen Numbers



(e) single crystal

K_{Ie} (MPa \sqrt{m})

1.5
1.4
1.3
1.2
1.1
1.0
0.9

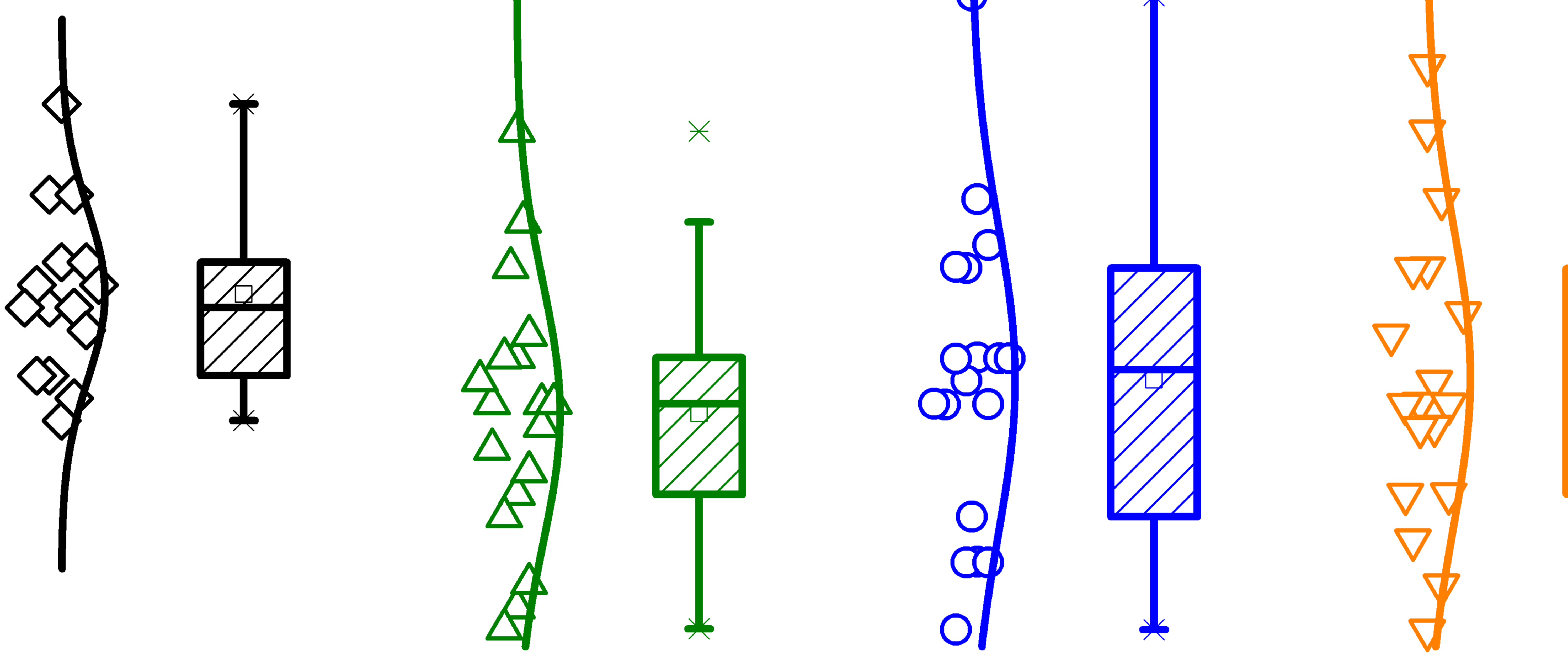
0

200

500

800

Hydrogen Numbers



(f) single crystal, $R = 2 \text{ \AA}$

$K_{Ie} \text{ (MPa}\sqrt{\text{m}})$

1.5
1.4
1.3
1.2
1.1
1.0
0.9

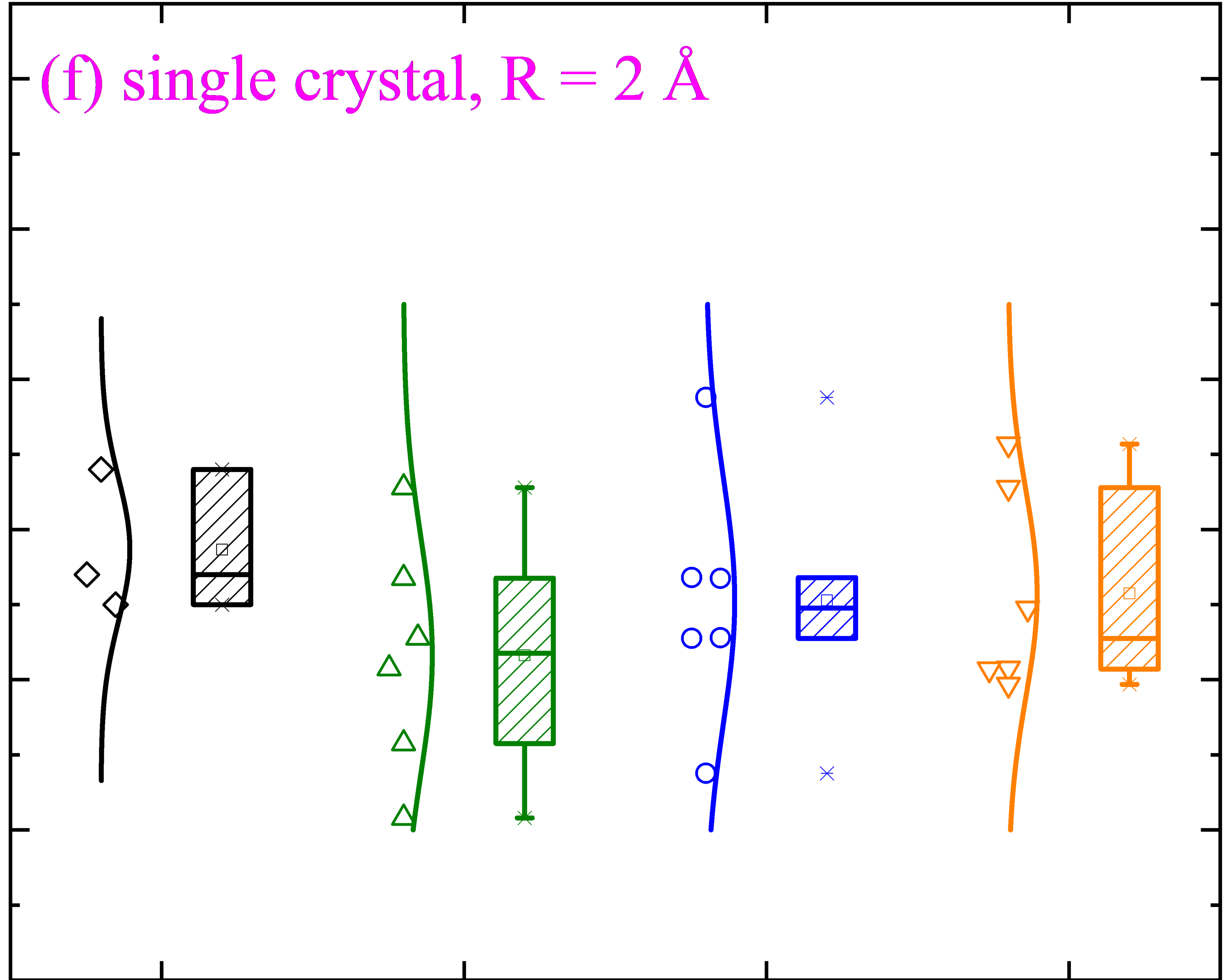
0

200

500

800

Hydrogen Numbers



(g) single crystal, $R = 5 \text{ \AA}$

K_{Ie} (MPa $\sqrt{\text{m}}$)

1.5
1.4
1.3
1.2
1.1
1.0
0.9

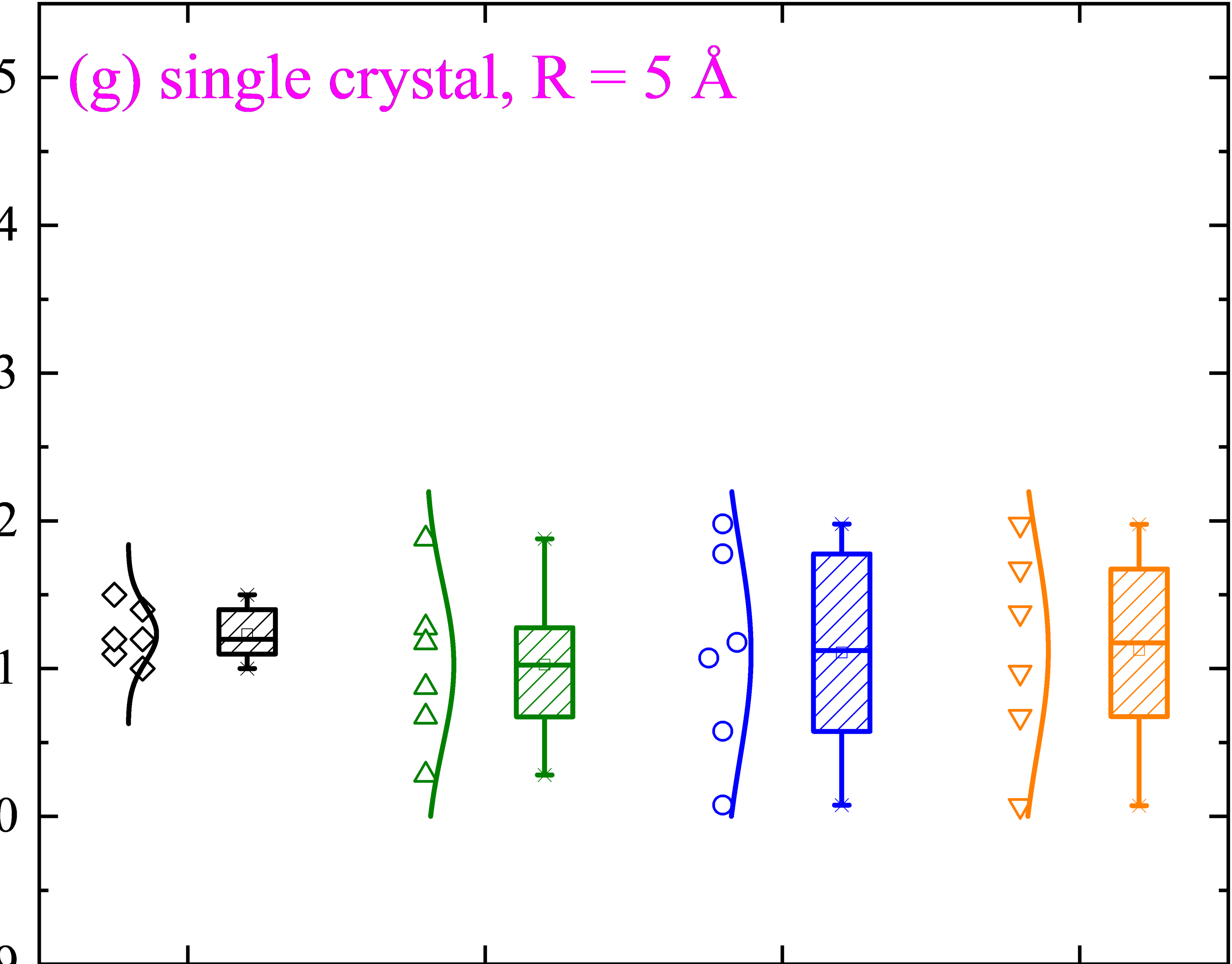
0

200

500

800

Hydrogen Numbers



(h) single crystal, $R = 8 \text{ \AA}$

K_{Ie} (MPa $\sqrt{\text{m}}$)

1.5
1.4
1.3
1.2
1.1
1.0
0.9

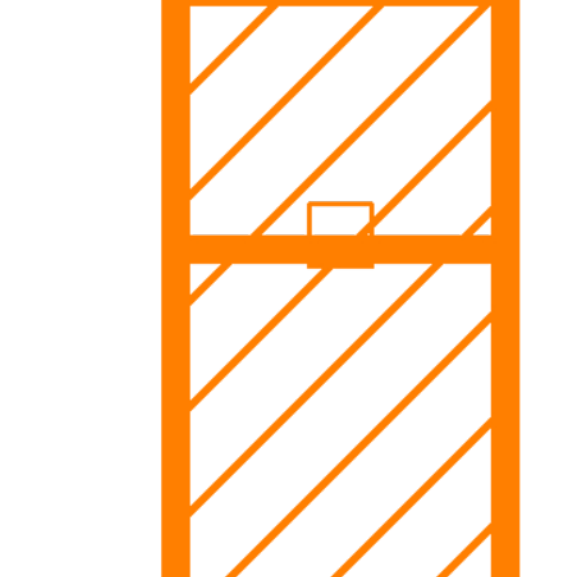
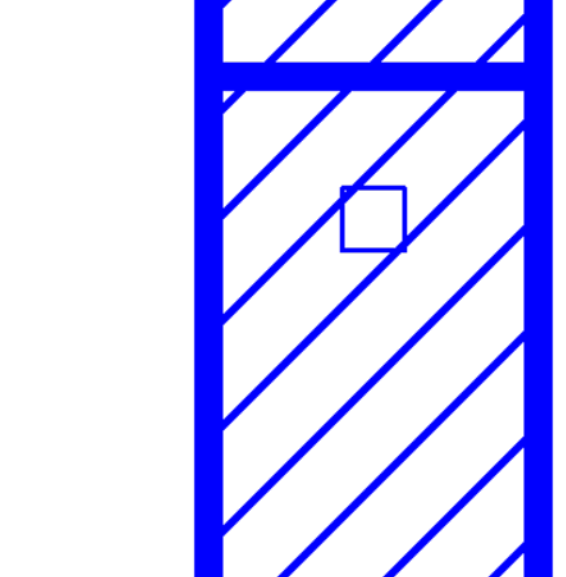
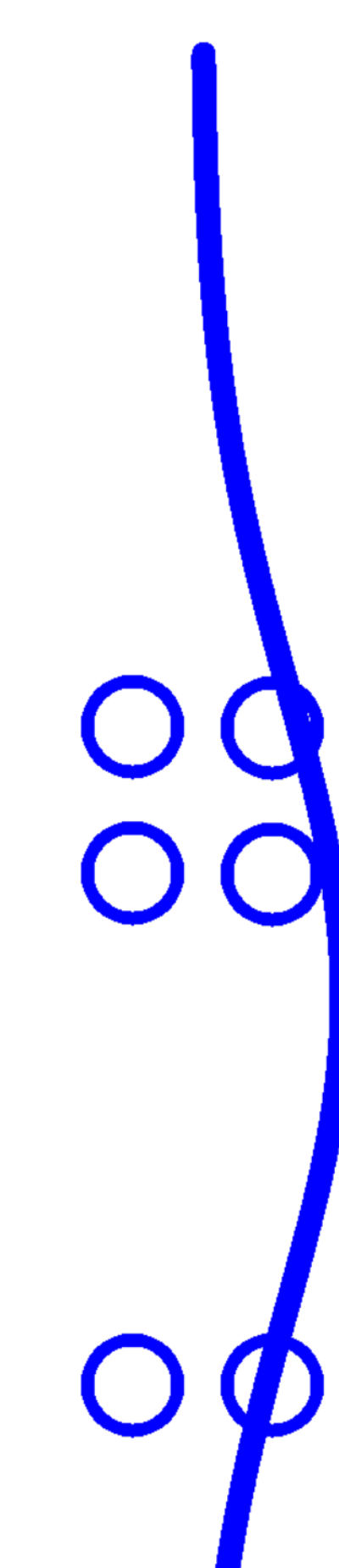
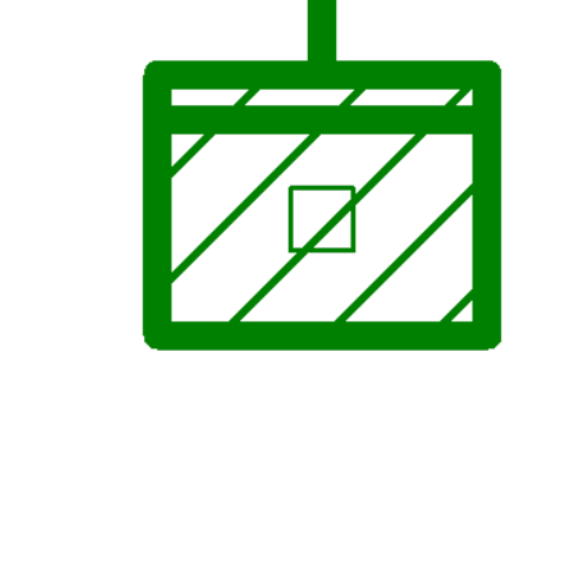
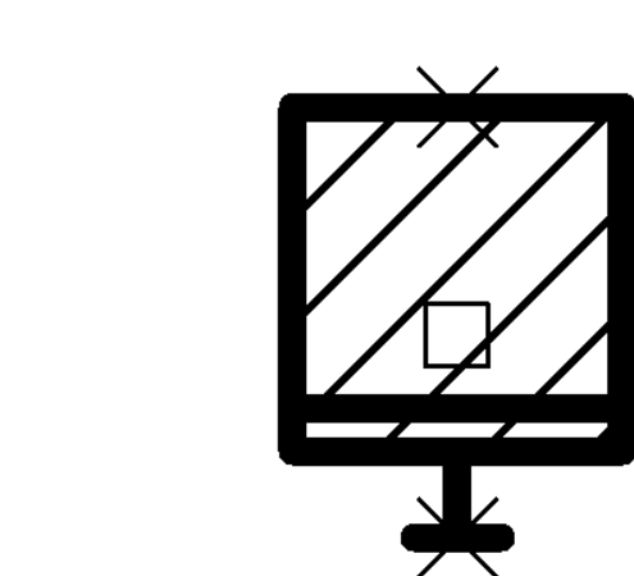
0

200

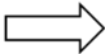
500

800

Hydrogen Numbers



Brittle cleavage



Ductile blunt



Semi-brittle

